Modeling and design of a PV-Fed SEPIC for maximum power point tracking with current mode control

Youssra Rais[1] | Kuntal Mandal[2] | Alia Zakriti[1] | Abdellatif Khamlichi[3] | Mohamed Al-Numay[4] | Abdelali El Aroudi[2]

[1]Research Unit of Advanced Science and Technology, ENSA of Tetouan, Abdelmalek Essaadi University Tetouan, Morocco.

[2]Department of Electronics, Electrical Engineering and Automatic Control, Universitat Rovira i Virgili, Tarragona, Spain.

[3]STIC Laboratory, Abdelmalek Essaadi University Tetouan, Morocco.

[4]Electrical Engineering Department, King Saud University, Riyadh, Saudi Arabia.

Correspondence

Youssra Rais, Research Unit of Advanced Science and Technology, ENSA of Tetouan, Abdelmalek Essaadi University, 2222 M'hannech, Tetouan,

Summary

In this work, the control of a Single Ended Primary Inductor Converter (SEPIC) supplied from a photovoltaic energy source and linked at its output to a DC current sink is addressed. The system is used for maximum power point tracking under varying environmental conditions. A strategy based on two loops of control is considered. A peak current mode controller is used for the inner loop and a Proportional-Integral (PI) controller is used for the outer voltage loop. Then, a comprehensive time-domain and frequency-domain modeling of the inner loop is theoretically addressed and then verified by the switched model of the system implemented in PSIM© software. The obtained results show that the system exhibits accurate tracking of the desired PV voltage while guaranteeing a fast maximum power point tracking under sudden changes in the environmental conditions. The mathematical modeling, design procedures, and the numerical simulations are validated using experimental results obtained from a laboratory prototype.

KEYWORDS

Solar PV energy, MPPT, DC-DC converter, Single-Ended Primary-Inductor Converter (SEPIC), small-signal modeling, Peak Current Mode Control (PCMC).

1 | INTRODUCTION

Solar Photovoltaic (PV) energy is one of the renewable energies which has received remarkable interest in the last decade [1–4]. The return on investment of PV systems has increased as a consequence of the PV panels and their associated components price reduction [5,6]. New PV technologies have emerged regarding materials like multi-crystalline silicon, thin films, and the multi-junction solar cells [7,8]. Important development has also been accomplished in power electronics needed for conditioning the power supplied to the loads. However, PV systems are known to suffer from a number of issues that limit their efficiency. The PV generated power fluctuates according to environmental conditions (irradiance, temperature, shading, soiling, etc…) [9]. This has the negative effect of introducing complications that impede efficient conversion of solar energy with the consequence of reducing the economic and social benefits of PV installations. To overcome these drawbacks, proper design and control of the PV systems is needed with the aim to enhance their overall performance and to compensate for the effects resulting from the external disturbances. Indeed, the $p - v$ (power-voltage) and $i - v$ (current-voltage) characteristic curves of a PV generator are highly

dependent on the environmental conditions [10], leading to a need for appropriate control of the PV voltage. An essential prerequisite in controlling PV systems is to permanently adapt the actual solar power source characteristics to the specifications of the load irrespective of environmental conditions [11] and to continuously extract the maximum power from the PV array. This is achieved generally by implementing a Maximum Power Point Tracking (MPPT) algorithm using a power electronics interface [12]. Various MPPT algorithms have been developed and have been widely reported in the literature [3].These include the Perturb and Observe (P&O) algorithm [13–15], the Fractional Open Circuit Voltage (FOCV) method [16–18], the Incremental Conductance (InC) algorithm [12,19], artificial intelligence based methods (Artificial Neural Networks, Fuzzy Logic,..) [20–22] and other biology inspired methods like the Particle Swarm Optimization (PSO) technique [23] and Genetic Algorithm (GA) [24]. However the most used algorithms in practice are the P&O and InC.

A DC-DC power converter is, hence, required to regulate and stabilize the output voltage generated by the PV array and implement the MPPT algorithm to meet the Maximum Power Point (MPP). To fulfill this function, the DC-DC converter should be adequately designed and controlled. So, improving the control design of DC-DC converters in general and in this kind of application in particular plays a key role as it can enable to monitor favorably most of the exogenous changes endured by the PV systems. Depending on applications, various topologies of DC-DC converters can be used in a PV system. The choice of a converter depends on the specific usage of the PV source. If one looks for a converter capable of producing a non-inverting output voltage that can be greater or less than the input voltage, then among the proposed topologies there are the Single Ended Primary Inductor Converter (SEPIC) and Zeta converters. These two converters have comparable switching stress and components count. However, in PV applications, the main requirement is a continuous current at the input port of the converter to perform MPPT. This requirement is fulfilled in the SEPIC converter because of the existence of an inductor at its input port while the input current of a ZETA converter is pulsating which can cause the reduction of the lifespan of PV arrays [26].

The particular topology of the SEPIC allows to step-up or to step-down the voltage at its output by means of adjusting the duty cycle of the square wave signal driving the converter main switch thus offering a significant compliance at any voltage level [27] and being able to sweep the entire $i - v$ curve of a PV source.

For closing the loop of the converter, either the voltage mode or the current mode control strategies can be used. To achieve MPPT, direct duty cycle control [28,29], voltage mode control [15,30] and two-loop current mode control [31–33] have been used. In direct duty cycle control the MPPT algorithm directly dictates the desired duty cycle for MPPT. The advantage of this approach is the simplicity of the scheme. However, the dynamic performances of this strategy are very poor and severe oscillatory behavior may be produced after any step change due the MPPT P&O algorithm (see for instance [29]). To overcome this problem, PV voltage regulation can be used [30]. The voltage-regulation-based MPPT techniques are the most widely used because of their robustness with respect to a sudden irradiance drop. The oscillatory behavior due to MPPT step changes may be appropriately damped [30]. However, the settling time could still be large.

The current-mode-based MPPT technique allows a faster convergence after each perturbation but a sudden drop in the irradiance might lead to the failure of the algorithm. This explains why most of the MPPT techniques found in the literature are based on regulating the PV voltage and only few studies about MPPT control based on the current exist in literature. Taking benefits from the robust performances and the fast system response guaranteed by sliding mode control, a P&O MPPT strategy using the current is introduced in [33] and applied to a boost converter. The problem with fast drop of irradiance is tracked by using in the feedback loop the input capacitor current which contains information about both the inductor current and the PV voltage. The same technique was applied in [34] to a SEPIC but the mathematical analysis was performed only on a reduced-order two-dimensional model of the converter. Moreover, how the model changes in terms

of the weather conditions was not discussed. In [35], the analysis and design of a novel P&O algorithm based on the sliding-mode control of the input inductor current of a SEPIC is presented for static installations with a DC constant voltage load without using PV voltage in the feedback loop. The proposed MPPT algorithm in [35] is appropriate for static installations where the power converters are interconnected in series or parallel and where meeting the constraints imposed by the interconnection and maximum power transfer in each converter module can be mitigated by output-series connected SEPICs with the proposed MPPT technique. Each converter in the interconnected system can operate in either buck or boost modes. The problem with the use of sliding-mode control approach is that the final implementation is carried out by using a hysteretic controller which leads to a variable switching frequency operation and which in turn makes the design of filter difficult.

Two-loop current mode control of SEPIC for MPPT was addressed in [36] designed for wind energy conversion system. The system was shown to perform both MPPT and voltage regulation at the wind generator output while guaranteeing tracking of the MPP under changes in the wind speed. However, only simulation results were shown and the modeling and design of the converter under varying weather conditions were not presented.

Like with other power converters used in PV systems, using the two-loop current mode control technique in a PV system, the SEPIC can perform both MPPT and voltage conditioning at the PV generator output while guaranteeing fast tracking of the MPP under sudden changes in the irradiance level or the temperature.

The two-loop control technique relies on two control loops in cascade, in the particular case of a PV system: an outer feedback loop for the PV voltage and an inner feedback loop for the input inductor current. The inner loop controls the inductor current and the outer loop regulates the PV voltage while providing the reference signal for the inner loop. This was found to behave well and to provide good performance with regards to transient response [37,38]. However, current mode control of high order converters such as the SEPIC is challenging even with constant voltage and a simple resistive load due to the high dimension of the system. For instance, in [39], the current loop stability of peak-current-controlled SEPIC was assessed where the sampling effects were ignored and peculiar instability phenomena have been reported. The sampling effects refers to the fact that duty cycle of the converter is a discrete-time variable that is decided only once per switching cycle. A current mode control for SEPIC in standalone PV system using the switch current is designed in [40], where the current reference is generated from the outer PV voltage loop. However, a reduced-order of the converter was used in the design and the sampling effects were not taken into account.

To accurately model the inner loop, using the inductor current, a large-signal model of this loop must be first obtained and from it the small-signal model must be derived, while considering the sampling effect at high frequencies associated to Peak Current Mode Control (PCMC) [37,38].

In this work, theoretical modeling and design of a PV-fed SEPIC is presented. A detailed modeling of PCMC for the converter is performed. Four large signal models from the literature [41–44] estimating the average inductor current behavior are studied. The transfer function corresponding to the sampling effect is developed for the four different models. A detailed comparison among these models is performed and the most accurate and simplest one is determined. Then, the MPPT performance associated to the outer loop PV voltage control with a conventional PI controller is studied for a standard PV generator. Finally, a parametric study is conducted under varying levels of solar irradiation and temperature. Numerical simulations and experimental measurements from a laboratory prototype are presented to validate the design procedures followed in this work.

The rest of the paper is organized as follows. Section 2 deals with the overall system description and its mathematical modeling. Section 3 addresses the PCMC modeling for the considered system. In Section 4,

the numerical simulation results are presented and discussed. In Section 5, experimental results are given to validate the numerical simulations and the theoretical findings. Finally, some concluding remarks are presented in the last section. As a notational convention adopted in this paper, the steady-state of the state variables and fixed parameters are indicated with capital letters. State variables are represented by small letters and small-signal perturbations are indicated by small hatted letters.

2 | SYSTEM OVERVIEW AND MATHEMATICAL MODELING

2.1 | Overall system description

The system under study in this work is a PV-fed SEPIC under PCMC to track the maximum power generated by a PV generator. The output of the SEPIC is connected to a constant current sink considered as a load. Note that for a resistive load the same design procedures followed in this paper can be applied. However, the design with a current sink as a load is more challenging since the power stage of the converter is not damped. In stand-alone application, an energy storage battery would be required along with a more sophisticated MPPT algorithm when there is no consumption of the harvested energy. Such an operation mode where the converter is used a battery charger is not considered here.

FIGURE 1 shows the circuit diagram of the system under study. The control approach is based on PCMC of the inductor L_1 current i_{L1} to generate the binary driving signal u that drives the switch S of the converter. The reference current is generated by the outer voltage mode controller and the reference signal of the latter is delivered by a P&O MPPT algorithm. The SEPIC is assumed operating in Continuous Conduction Mode (CCM). The switch S is closed during the time interval $[nT_s, (n+d)T_s], n \in \mathbb{N}$ and it is open during the time interval $[(n+d)T_s, (n+1)T_s], n \in \mathbb{N}$, where d is the duty cycle of the driving signal u and T_s is the switching period.

The inner current loop comprises, as depicted in FIGURE 1, a sensing resistor R_s, a comparator, and an RS flip-flop. The switching frequency $f_s = 1/T_s$ is set by a T_s −periodic clock signal applied to the set entry of the RS flip-flop. The current of the first inductor i_{L1}, sensed via the sensing resistor R_s, is added to an external compensation ramp v_m with a slope $m_a = V_m/T_s$, where V_m is its amplitude. The sum signal $R_s i_{L1} + v_m$ is compared to the reference $R_s i_{ref}$ generated by the outer voltage loop. The comparator output signal is supplied to the reset entry of the flip-flop. During $[nT_s, (n+d)T_s], n \in \mathbb{N}$, the switch S is closed and the current i_{L1} increases, when the signal $R_s i_{L1} + v_m$ attains the value of $R_s i_{ref}$, the output signal of the comparator (Reset) becomes a logic high, which resets the control signal of the switch S to a logic low. Once S is open, i_{L1} decreases during $[(n+d)T_s, (n+1)T_s], n \in \mathbb{N}$ until the next rising edge of the clock signal. The state of the diode D is complementary to that of the switch S.

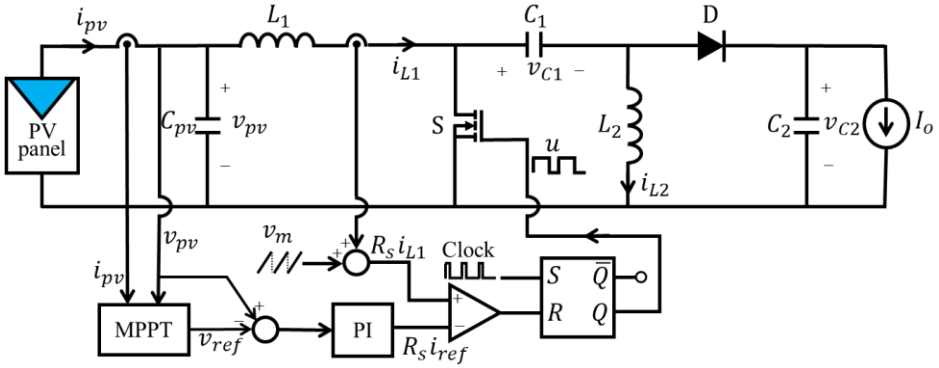

FIGURE 1 Circuit diagram of the PV-fed SEPIC connected to a constant current sink under PCMC for MPPT.

In the scope of a linear controller design, keeping in mind that the MPPT controller will force the system to operate at the MPP, the nonlinear $i - v$ characteristic equation of the PV source can be approximated in the close vicinity of the MPP using the linear Norton equivalent model as given by the following equation, assuming slowly changing temperature and irradiance quantities [45]:

$$i_{pv} \approx 2I_{mpp} - G_p v_{pv} \tag{1}$$

where $G_p = I_{mpp}/V_{mpp}$ is the equivalent Norton conductance, I_{mpp} and V_{mpp} are the PV generator current and voltage at the MPP.

Hence the resulted circuit of the PV generator linear equivalent model, at the MPP, is incorporated with the circuit diagram of the SEPIC and the aforementioned current sink. The circuit topology corresponding to the ON switching state is shown in FIGURE 2(a) and the one corresponding to the OFF switching state is illustrated in FIGURE 2(b), where $I_N = 2I_{mpp}$ is the Norton equivalent current and $R_N = 1/G_p = V_{mpp}/I_{mpp}$ is the Norton equivalent parallel resistance.

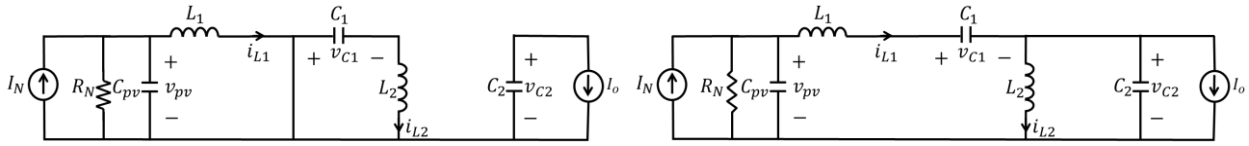

(a) (b)

FIGURE 2 The two switched sub-circuits of the PV-fed SEPIC: (a) during $[nT_s, (n+d)T_s]$ and (b) during $[(n+d)T_s, (n+1)T_s]$.

2.2 | SEPIC power stage parameters design

Inductances L_1 and L_2 values

In steady-state, the peak-to-peak current ripple of the inductors L_1 and L_2 are as given by the following expressions:

$$\Delta i_{L1} = \frac{V_{pv} D}{L_1 f_s}$$
$$\Delta i_{L2} = \frac{V_{pv} D}{L_2 f_s} \tag{2}$$

The allowed current ripples for the considered SEPIC are less than 30% of their steady-state average values *i.e.,* $\Delta i_{L1} \leq 0.3 I_{L1}$ and $\Delta i_{L2} \leq 0.3 I_{L2}$. Using the steady-state expression of I_{L1} and I_{L2} the following constraints are obtained:

$$L_1 \geq \frac{V_{pv}(1-D)}{0.3 I_o f_s}$$
$$L_2 \geq \frac{V_{pv} D}{0.3 I_o f_s} \tag{3}$$

Hence, the minimum values of L_1 and L_2 satisfying the above conditions are given by (4).

$$(V_{pv}(1-D)) \tag{4}$$

$$L_{2min} = \frac{(V_{pv}D)_{max}}{0.3I_o f_s}$$

As mentioned in [46], for the SEPIC to operate in the CCM, the inductances L_1 and L_2 should satisfy the condition in (5):

$$(1-D)^2 < K \tag{5}$$

where $K = (2L_1L_2)/(R_oT_s(L_2 - L_1))$ and $R_o = V_{C2}/I_o$.

The PV-fed SEPIC will operate in CCM for all duty cycle values if $K > 1$. By selecting $L_1 = L_2$, CCM operation will be guaranteed for all steady-state duty cycle values and therefore under all temperature and irradiance values.

Capacitances C_1 and C_2 values

In steady-state, the peak to peak voltage ripple of the capacitors $C_1$and C_2 are:

$$\begin{aligned} \Delta v_{C1} &= \frac{(1-D)I_{L1}}{C_1 f_s} \\ \Delta v_{C2} &= \frac{I_o D}{C_2 f_s} \end{aligned} \tag{6}$$

The allowed voltage ripples for the capacitors C_1 and C_2 are chosen less than 3% of their steady-state average values *i.e,* $\Delta v_{C1} \leq 0.03V_{C1}$ and $\Delta v_{C2} \leq 0.03V_{C2}$. Therefore, the minimum values of $C_1$and C_2 are as given by the following expressions:

$$\begin{aligned} C_{1min} &= \left(\frac{D}{V_{pv}}\right)_{max} \frac{I_o}{0.03 f_s} \\ C_{2min} &= \left(\frac{1-D}{V_{pv}}\right)_{max} \frac{I_o}{0.03 f_s} \end{aligned} \tag{7}$$

2.3 | PV-fed SEPIC dynamics

Based on the switched sub-circuits depicted in FIGURE 2, the PV-fed SEPIC can be mathematically described by applying the Kirchhoff laws and averaging the resulting switched model during one switching period T_s. Hence, the averaged equations describing the converter dynamics are:

$$\frac{di_{L1}}{dt} = \frac{v_{pv}}{L_1} - \frac{v_{C1}}{L_1} + \frac{v_{C2}}{L_1} \tag{8}$$

$$\frac{dv_{C2}}{dt} = \frac{-I_o}{C_2} d + \frac{i_{L1} - i_{L2}}{C_2} - \frac{I_o}{C_2}$$

where all the variables and parameters can be identified in FIGURE 2.

2.4 Steady-state inductor currents and capacitor voltages

In order to obtain the steady-state inductor currents and capacitor voltages, the voltage-second balance for the inductors and the charge-second balance for the capacitors principles [47] are applied, which result in the following expressions for the steady-state average values:

$$\begin{aligned} I_{L1} &= \frac{D}{D'} I_o = I_{mpp} \\ I_{L2} &= -I_o \\ V_{pv} &= R_N \left(I_N - \frac{D}{D'} I_o \right) = R_N I_{mpp} = V_{mpp} \\ V_{C1} &= R_N \left(I_N - \frac{D}{D'} I_o \right) = V_{mpp} \\ V_{C2} &= \frac{D}{D'} R_N \left(I_N - \frac{D}{D'} I_o \right) = \frac{D}{D'} V_{mpp} \end{aligned} \tag{9}$$

It is worth to note that for the SEPIC fed by a current source and loaded by a constant current sink, the steady-state duty cycle is given by $D = \frac{I_{mpp}}{I_{mpp} + I_o}$.

2.5 | The control-to-inductor current open-loop transfer function

The state-space modeling and the small-signal analysis were performed [47] to obtain the open-loop control-to-inductor current ($\hat{d}$ − to $-\hat{\imath}_{L1}$) transfer function, presented in equation (10).

$$H_{id}(s) = \frac{1}{D'^2} \frac{b_4 s^4 + b_3 s^3 + b_2 s^2 + b_1 s + b_0}{a_5 s^5 + a_4 s^4 + a_3 s^3 + a_2 s^2 + a_1 s + a_0} \tag{10}$$

where s is the Laplace variable, D is the steady-state duty cycle, $D' = 1 - D$, and the coefficients $a_0, a_1, a_2, a_3, a_4, a_5, b_0, b_1, b_2, b_3$ and b_4 are as given by the following expressions:

$a_0 = D'^2,\ a_1 = R_N\big((C_1 + C_{pv})D'^2 + C_2 D^2\big),\ a_2 = (C_1 L_s + C_2 L_2)D'^2 + C_2 L_1 D^2,$
$a_3 = R_N \left(C_{pv}(C_1(L_1 + L_2) + C_2 L_2)D'^2 + C_2\big(C_1 L_2 + C_{pv} L_1 D^2\big)\right),\ a_4 = C_1 C_2 L_1 L_2,$
$a_5 = C_1 C_2 C_{pv} L_1 L_2 R_N,$
$b_0 = I_o D'^2,\ b_1 = R_N\ ((C_1 + C_{pv})D'^2 + C_2 D^2),\ b_2 = (C_1 + C_2)L_2 I_o D'^2 + C_2 C_{pv} R^2{}_N D(I_N D' - I_o D),$
$b_3 = ((C_1 + C_2)C_{pv} I_o D'^2 + C_1 C_2(D' I_N - D I_o))\ L_2 R_N,\ b_4 = C_1 C_2 C_{pv} L_2 R^2{}_N(D' I_N - I_o D).$

2.6 | Validation of the mathematical model

To validate the obtained mathematical model, the 'Sunmodule Plus SW 255 mono' PV panel is used in numerical simulations with the values listed in TABLE 1 under Standard Test Conditions (STC).

TABLE 1 'Sunmodule Plus SW 255 mono' performance under STC (1000 W/m², 25 °C, AM 1.5).

Maximum power	P_{mpp}	255 W

Open circuit voltage	V_{oc}	37.8 V
Maximum power point voltage	V_{mpp}	31.4 V
Short circuit current	I_{sc}	8.66 A
Maximum power point current	I_{mpp}	8.15 A

The $p-v$ and $i-v$ characteristic curves of the PV panel, obtained from PSIM© software for several irradiance levels with constant temperature are shown in FIGURE 3(a) while the same curves for different temperature values and fixed irradiance are depicted in FIGURE 3(b). Hence, the MPP parameters were extracted for the different irradiance and temperature sets in order to calculate the corresponding Norton model and the corresponding duty cycle, as shown in TABLE 2.

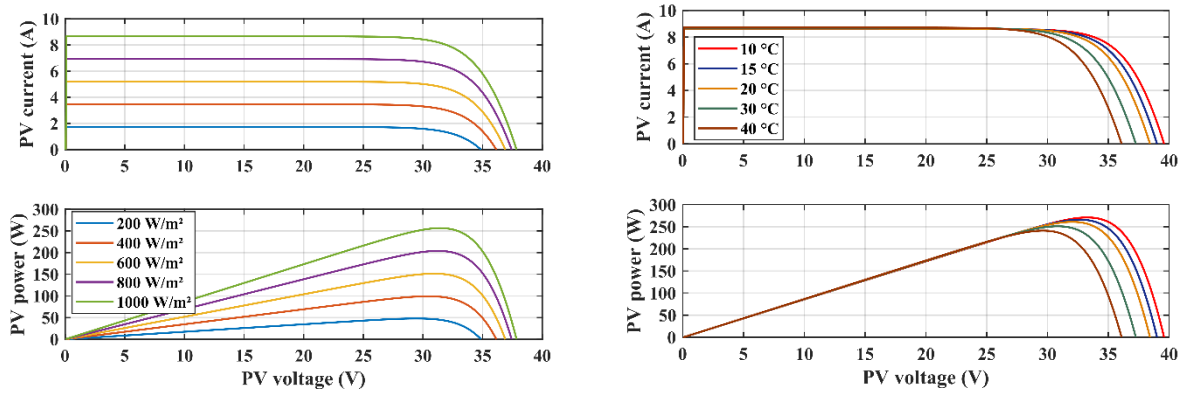

(a) (b)

FIGURE 3 The i–v and p–v curves of the Sunmodule Plus SW 255 PV panel: (a) for temperature 25 °C and (b) for irradiance 1000 W/m².

TABLE 2 PV generator parameters and its steady-state duty cycle for different irradiance and temperature values.

Irradiance (W/m²)	Temperature (°C)	V_{mpp} (V)	I_{mpp} (A)	P_{mpp} (W)	I_N (A)	R_N (Ω)	D
1000	25	31.30	8.16	255.39	16.32	3.84	0.67
800	25	31.15	6.53	203.27	13.06	4.77	0.62
600	25	30.85	4.89	151.10	9.78	6.31	0.55
400	25	30.45	3.26	99.10	6.52	9.34	0.45
200	25	29.40	1.63	47.86	3.26	18.04	0.29
1000	10	33.25	8.16	271	16.32	4.17	0.68
1000	15	32.65	8.16	266	16.32	4.00	0.67
1000	20	32.05	8.16	261.10	16.32	3.93	0.67
1000	30	30.85	8.15	251.13	16.30	3.87	0.68
1000	40	29.60	8.17	271	16.32	3.63	0.67

The SEPIC parameters selected using the expressions obtained in (4) and (7) are shown in TABLE 3. They were used in conjunction with the parameters given in TABLE 2 to derive the numerical values of the $H_{id}(s)$ coefficients and to implement the circuit-based switched model in PSIM© software.

TABLE 3 Circuit parameters.

	Parameters	Values
SEPIC parameters	L_1	580 µH
	L_2	580 µH

	C_1	1 µF
	C_2	47 µF
Input capacitor	$\boldsymbol{C_{pv}}$	25 µF
Output load current	I_o	4 A
Switching frequency	$\boldsymbol{f_s}$	100 kHz

Afterwards, the bode diagrams of $H_{id}(s)$ transfer function given in (10), corresponding to different irradiance and temperature sets, were obtained by means of MATLAB© calculations. The frequency responses corresponding to the same transfer function were obtained from the switched model implemented in PSIM© software using the AC sweep tool. All the obtained bode plots from MATLAB© calculations and frequency responses from AC sweep of PSIM© software are shown in FIGURE 4(a) and FIGURE 4(b).

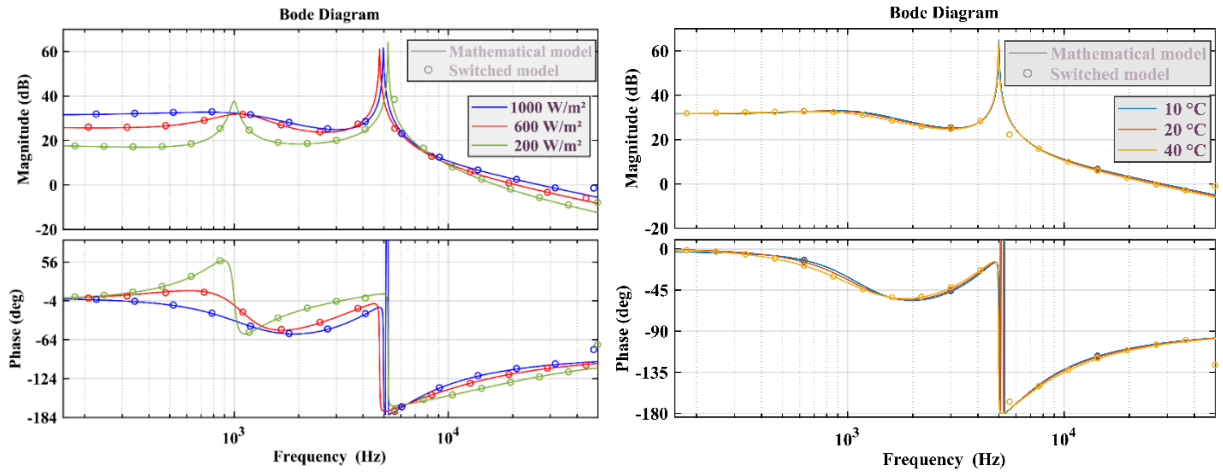

(a) (b)

FIGURE 4 The obtained frequency responses of H_{id} from the mathematical model and from the switched model: (a) for temperature 25 °C and variable irradiance and (b) for irradiance 1000 W/m² and variable temperature.

The results show a very close agreement between the obtained mathematical transfer functions and the circuit-based simulations in PSIM© software using AC sweep tool. Therefore, the obtained model can be used for control design of the PV-fed SEPIC under PCMC. It is worth to note that the variation of temperature has a negligible effect on the transfer functions as can be observed in FIGURE 4 (b).

The steady-state average values of the state variables are calculated using the derived mathematical expressions in (9) and are also extracted using the switched model for different values of irradiance and a constant temperature. The obtained numerical results are listed in TABLE 4.

TABLE 4 The obtained steady-state numerical values of the state variables.

	200 W/m²		**600 W/m²**		**1000 W/m²**	
	Mathematical model	**Switched model**	**Mathematical model**	**Switched model**	**Mathematical model**	**Switched model**
I_{L1} (A)	1.63	1.63	4.89	4.89	8.16	8.17
I_{L2} (A)	-4.00	-3.99	-4.00	-3.99	-4.00	-4.00
V_{pv} (V)	29.34	29.37	30.86	30.85	31.29	31.26
V_{C1} (V)	29.34	29.37	30.86	30.85	31.29	31.26
V_{C2} (V)	11.98	11.97	37.72	37.71	63.85	63.83

As can be observed from TABLE 5, the values obtained from the two models are in a remarkable agreement for all the considered irradiance levels which validate the steady-state analysis performed previously.

3 | PV-FED SEPIC UNDER PEAK CURRENT MODE CONTROL

3.1 | INNER CURRENT LOOP MODELING

3.1.1 | Averaged value of the inductor current i_{L1}

In order to derive the averaged value of the inductor current i_{L1} under PCMC in CCM operation, the waveform of this current is considered during one switching period, see FIGURE 5. Within this scope, four approaches proposed in [41–44] are used and compared. The mathematical equations are developed according to the aforementioned four approaches that are applied, in the present work, to the PV-fed SEPIC.

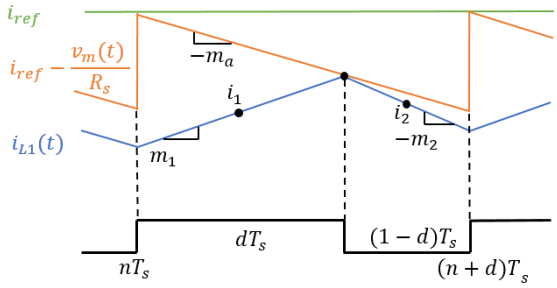

FIGURE 5 Currents waveforms including the compensation ramp under PCMC.

According to [41], the inductor current average value $\langle i_{L1} \rangle$ can be approximated by the following equation:

$$\langle i_{L1} \rangle = i_1 = i_{ref} - m_a dT_s - \frac{1}{2} m_1 dT_s \tag{11}$$

where m_1 is the inductor current slope during the ON-mode time and it is given by the following equation:

$$m_1 = \frac{v_{pv}}{L_1} \tag{12}$$

In [42], the average inductor current is approximated considering the OFF-mode time subinterval as follows (13):

$$\langle i_{L1} \rangle = i_2 = i_{ref} - m_a dT_s - \frac{1}{2} m_2 (1-d) T_s \tag{13}$$

where m_2 is the inductor current slope during the OFF-mode time subinterval and it is given by the following equation:

$$m_2 = -\frac{v_{pv} - v_{C1} - v_{C2}}{L_1} \tag{14}$$

Another approximation of $\langle i_{L1} \rangle$ was proposed in [43] using weighted average of i_1 and i_2 as given by:

$$\langle i_{L1} \rangle = d i_1 + (1-d) i_2 \tag{15}$$

By substituting i_1 and i_2 by their expressions in (11) and (13), $\langle i_{L1} \rangle$ in (15) becomes as follows:

$$\langle i_{L1}\rangle = i_{ref} - m_a d^2 T_s - \frac{1}{2} m_2 (1-d)^2 T_s \tag{16}$$

A different approach using also the weighted average of $i_1$and i_2 is presented in [44] and it came up with another expression estimating $\langle i_{L1}\rangle$ which is given below:

$$\langle i_{L1}\rangle = (1-d) i_1 + d i_2 \tag{17}$$

and which after substitution of $i_1$and i_2 becomes:

$$\langle i_{L1}\rangle = i_{ref} - m_a d T_s - \frac{1}{2}(m_1 + m_2) d(1-d) T_s \tag{18}$$

The four expressions derived using the abovementioned approaches [41–44] are summarized in TABLE 6:

TABLE 6 The four expressions of $\langle i_{L1}\rangle$ following the four approaches presented in [41–44].

Model 1 [41]	$\langle i_{L1}\rangle = i_{ref} - m_a d T_s - \frac{1}{2} m_1 d T_s$	(19)
Model 2 [42]	$\langle i_{L1}\rangle = i_{ref} - m_a d T_s - \frac{1}{2} m_2 (1-d) T_s$	(20)
Model 3 [43]	$\langle i_{L1}\rangle = i_{ref} - m_a d^2 T_s - \frac{1}{2} m_2 (1-d)^2 T_s$	(21)
Model 4 [44]	$\langle i_{L1}\rangle = i_{ref} - m_a d T_s - \frac{1}{2}(m_1 + m_2) d(1-d) T_s$	(22)

3.1.2 | Small-signal Modeling

The small-signal models are developed for the four above-mentioned expressions of $\langle i_{L1}\rangle$ by perturbing and linearizing the large-signal equations (11), (13), (16) and (18). This will result in the small-signal control law under PCMC. The small-signal duty cycle $\hat{d}$ is then deduced for the four models, as shown in TABLE 7, after substituting $\hat{m}_1$and $\hat{m}_2$ by their expressions using (12) and (14). The artificial ramp slope m_a is assumed to be constant and equal to M_a.

TABLE 7 Small-signal expressions of the duty cycle under PCMC.

Model 1 [41]	$\hat{d} = \frac{1}{\left(M_a + \frac{1}{2} M_1\right) T_s}\left(\hat{\imath}_{ref} - \hat{\imath}_{L1} - \frac{1}{2L_1}\hat{v}_{pv} D T_s\right)$	(23)
Model 2 [42]	$\hat{d} = \frac{1}{\left(M_a - \frac{1}{2} M_2\right) T_s}\left(\hat{\imath}_{ref} - \hat{\imath}_{L1} + \frac{1}{2L_1}(\hat{v}_{pv} - \hat{v}_{C1} - \hat{v}_{C2}) D' T_s\right)$	(24)
Model 3 [43]	$\hat{d} = \frac{1}{M_a T_s}\left(\hat{\imath}_{ref} - \hat{\imath}_{L1} - \frac{D^2 T_s}{2L_1}\hat{v}_{pv} + \frac{D'^2 T_s}{2}(\hat{v}_{pv} - \hat{v}_{C1} - \hat{v}_{C2})\right)$	(25)
Model 4 [44]	$\hat{d} = \frac{1}{\left(M_a + \frac{(M_1 - M_2)}{2}\right) T_s}\left(\hat{\imath}_{ref} - \hat{\imath}_{L_1} - \frac{1}{2L_1}\left(2\hat{v}_{pv} - \hat{v}_{C1} - \hat{v}_{C2}\right) D D' T_s\right)$	(26)

where D is the steady-state value of the duty cycle under PCMC that is to be determined below.

3.1.3 | Steady-state duty cycle under PCMC

Under PCMC, the duty cycle steady-state value D is dependent on the parameters of the closed-loop PV-fed SEPIC circuit. Therefore, it is necessary to obtain its expression regarding other parameters in order to further develop the inner current loop modeling.

Using (11) for steady-state quantities, one gets the following equation expressing the steady-state value of the inductor current for Model 1 derived from [41]:

$$I_{L1} = I_{ref} - M_a D T_s - \frac{1}{2} M_1 D T_s \tag{27}$$

Taking into account that $M_1 = \frac{V_{pv}}{L_1}$, and using the steady-state expressions in (9) one obtains:

$$\frac{I_o D}{D'} = I_{ref} - M_a D T_s - \frac{1}{2L_1}(R_N I_N - \frac{D R_N I_o}{D'}) D T_s \tag{28}$$

By rearranging the above equation to desired form, D is found to be one of the solutions of the following quadratic equation in terms of D:

$$pD^2 + qD + r = 0 \tag{29}$$

where $p = [2L_1 M_a + R_N(I_N + I_o)]T_s$, $q = -(2L_1 M_a + R_N I_N)T_s - 2L_1(I_o + I_{ref})$ and $r = 2L_1 I_{ref}$.

The steady-state value of duty cycle D is the solution that fulfils the condition $0 < D < 1$.

By proceeding in the same way, one obtains for the other models the results depicted in TABLE 8.

TABLE 8 Equations of the steady-state duty cycle average value.

Model 1 [41]	$\frac{I_o D}{D'} = I_{ref} - M_a D T_s - \frac{1}{2} M_1 D T_s$	(30)
Model 2 [42]	$\frac{I_o D}{D'} = I_{ref} - M_a D T_s - \frac{1}{2} M_2 D' T_s$	(31)
Model 3 [43]	$\frac{I_o D}{D'} = I_{ref} - M_a D^2 T_s - \frac{1}{2} M_2 D'^2 T_s$	(32)
Model 4 [44]	$\frac{I_o D}{D'} = I_{ref} - M_a D T_s - \frac{1}{2}(M_1 + M_2) D D' T_s$	(33)

After expanding equations (30), (31), (32) and (33) and taking into consideration the steady-state average value of m_2 : $M_2 = \frac{V_{C2}}{L_1}$, it is obtained that D is the solution of the same equation (29) for all the four models.

3.1.4 | Transfer function of the inner loop

The small-signal transfer functions defining the relationship between the system state variables considered as outputs and the duty-cycle (input) are defined according to the following expressions:

$$\begin{aligned} \hat{\imath}_{L1}(s)|_{\hat{\imath}_{cu}=\mathbf{0}} &= H_{id}(s)\hat{d}(s) \\ \hat{v}_{pv}(s)\big|_{\hat{\imath}_{cu}=\mathbf{0}} &= H_{vd}(s)\hat{d}(s) \\ \hat{v}_{C1}(s)|_{\hat{\imath}_{cu}=\mathbf{0}} &= H_{1d}(s)\hat{d}(s) \\ \hat{v}_{C2}(s)|_{\hat{\imath}_{cu}=\mathbf{0}} &= H_{2d}(s)\hat{d}(s) \end{aligned} \tag{34}$$

where $i_{cu} = \begin{pmatrix} I_N \\ I_o \end{pmatrix}$, $H_{vd}(s)$, $H_{1d}(s)$ and $H_{2d}(s)$ are, respectively, the $\hat{d} -$ to$-\ \hat{v}_{pv}$, $\hat{d} -$ to$-\ \hat{v}_{c1}$ and $\hat{d} -$ to$-\ \hat{v}_{C2}$ transfer functions.

Applying the Laplace transform to the small-signal expressions of the duty cycle for the four models ((23), (24), (25) and (26)), and substituting the obtained result corresponding to each model in (34), one arrives to the following low-frequency small-signal control law under PCMC:

$$\hat{d}(s) = \frac{F_m}{1 + F_m\left(H_{id}(s) + F_{pv}H_{vd}(s) + F_1H_{1d}(s) + F_2H_{2d}(s)\right)}\hat{\imath}_{ref}(s) \tag{35}$$

where the modulator gains F_m, and the voltage gains F_{pv}, F_1 and F_2 for the four different approaches are listed in TABLE 9:

TABLE 9 The expressions of the different gains in (35).

	F_m	F_{pv}	F_1	F_2
Model 1	$\frac{1}{\left(M_a + \frac{1}{2}M_1\right)T_s}$	$\frac{DT_s}{2L_1}$	0	0
Model 2	$\frac{1}{\left(M_a - \frac{1}{2}M_2\right)T_s}$	$\frac{-(1-D)T_s}{2L_1}$	$\frac{(1-D)T_s}{2L_1}$	$\frac{(1-D)T_s}{2L_1}$
Model 3	$\frac{1}{M_aT_s}$	$\frac{(D^2-(1-D)^2)T_s}{2L_1}$	$\frac{(1-D)^2T_s}{2L_1}$	$\frac{(1-D)^2T_s}{2L_1}$
Model 4	$\frac{1}{\left(M_a + \frac{(M_1-M_2)}{2}\right)T_s}$	0	$\frac{D(1-D)T_s}{2L_1}$	$\frac{D(1-D)T_s}{2L_1}$

The expression $\hat{v}_{pv}(s)\big|_{\hat{\imath}_{cu}=0} = H_{pvd}(s)\hat{d}(s)$ is used to calculate the $\hat{\imath}_{ref}$ −to−$\hat{v}_{pv}$ transfer function, where $\hat{d}$ is substituted by its expression from the previous small-signal control law for each model ((23), (24), (25) and (26)). Thus, the control-to-output transfer function ($\hat{\imath}_{ref}$ −to−$\hat{v}_{pv}$) for the inner current loop is given for the four models by the following expression:

$$\frac{\hat{v}_{pv}(s)}{\hat{\imath}_{ref}(s)} = \frac{H_{vd}(s)F_m}{1 + F_m\left(H_{id}(s) + F_{pv}H_{vd}(s) + F_1H_{1d}(s) + F_2H_{2d}(s)\right)} \tag{36}$$

3.1.5 | Sampling effect modeling

Due to the sampling effects associated to PCMC, the sampled-data modeling should be used to precisely predict the dynamics of the converter at high frequencies [47]. Below, the sampled-data transfer function will be derived for the considered PV-fed SEPIC. Details will be provided for Model 1 and the same procedure can be followed to derive the sampling effect transfer function for the other models. In order to include the sampling effect model in the inner current loop, the current gain $H_{id}(s)$ will be substituted by $H_{se}(s)H_{id}(s)$ [42] where $H_{se}(s)$ is the transfer function that models the sampling effect. The same reasoning of [41] is used and the following considerations are taken into account for high frequencies [47,42]:

- $\hat{v}_{pv}, \hat{v}_{C_1}, \hat{v}_{C_2} \approx 0$ and hence, $\hat{m}_1, \hat{m}_2 \approx 0$. Therefore, the inductor L_1 current slopes are equal to their DC components M_1 and M_2 [47].
- At high frequencies, the $\hat{d}$ −to−$\hat{\imath}_{L1}$ transfer function can be approximated by: $H_{idhf} = \frac{M_1+M_2}{s}$. In order to validate this approximation for the system under study, the frequency response corresponding to H_{id} and H_{idhf} are plotted in FIGURE 6 for two irradiance values (200 W/m² and 1000 W/m²) while the temperature is kept constant (25 °C). As can be observed, the frequency responses are almost identical at high frequencies.

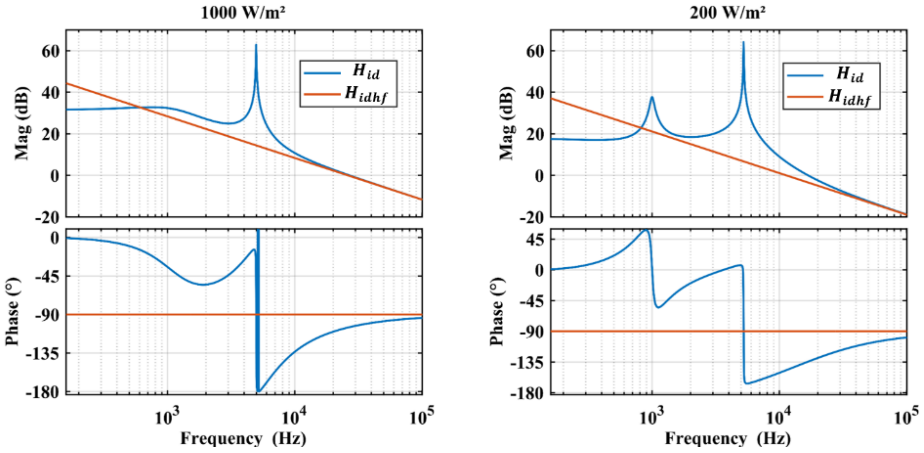

FIGURE 6 Bode plots of $\boldsymbol{H_{id}(s)}$ and $\boldsymbol{H_{idhf}(s)}$ for fixed temperature value: **25** °C and irradiance values: **1000** W/m² and **200** W/m².

At high frequency one gets, using (34), $\hat{\imath}_{L_1}(s)\big|_{\hat{\imath}_{cu}=0} = H_{id_{hf}}(s)\hat{d}(s)$. Therefore, substituting $H_{id}(s)$ by $H_{se}(s)H_{id}(s)$ in the expression of $\hat{d}$ in (35) for Model 1 one obtains the following $\hat{\imath}_{ref}$ −to−$\hat{\imath}_{L1}$transfer function:

$$\frac{\hat{\imath}_{L_1}(s)}{\hat{\imath}_{ref}(s)} = \frac{H_{id_{hf}}(s)F_{m1}}{1 + F_{m1}\, H_{se1}(s)H_{id_{hf}}(s)} \tag{37}$$

The previous transfer function can also be considered under discrete-time modeling. This was performed in [47] and the result found is:

$$\hat{\imath}_{L_1}[n] = \alpha\hat{\imath}_{L_1}[n-1] + (1-\alpha)\hat{\imath}_{ref}[n] \tag{38}$$

where $\alpha = -\frac{M_2 - M_a}{M_1 + M_a}$ is the discrete-time pole of the system under PCMC. By applying the z −transform, the discrete-time $\hat{\imath}_{ref}$ − to − $\hat{\imath}_{L_1}$ transfer function is obtained. Then, by substituting z by e^{sT_s} the conversion from the z-domain to the s-domain is performed. The sampled-data effect is modeled by a zero-order hold transfer function given by $\frac{1-e^{-sT_s}}{s}$ [47]. Using the approach in [48], the previous calculations result in the following $\hat{\imath}_{ref}$ − to− $\hat{\imath}_{L_1}$ transfer function in the s-domain:

$$\frac{\hat{\imath}_{L_1}(s)}{\hat{\imath}_{ref}(s)} = \frac{1-\alpha}{1-\alpha e^{-sT_s}}\frac{1-e^{-sT_s}}{sT_s} \tag{39}$$

The transfer function $H_{se1}(s)$ can be deduced by equating (37) and (39) which results in:

$$H_{se1}(s) = \frac{1}{F_{m1}H_{id_{hf}}(s)}\left(\frac{F_{m1}H_{id_{hf}}(s)(1-\alpha e^{-sT_s})}{(1-\alpha)(1-e^{-sT_s})}sT_s - 1\right) \tag{40}$$

This transfer function is particularized for Model 1, Model 2, Model 3 and Model 4 using their modulator gains F_{m1}, F_{m2}, F_{m3} and F_{m4} respectively.

Now the sampling effect transfer function $H_{se}(s)$ can be incorporated into (36) by substituting $H_{id}(s)$ as mentioned earlier. Consequently, (36) becomes:

$$\frac{\hat{v}_{pv}(s)}{\hat{\imath}_{ref}(s)} = \frac{H_{vd}(s)F_m}{1 + F_m\left(H_{se}(s)H_{id}(s) + F_{pv}H_{vd}(s) + F_1H_{1d}(s) + F_2H_{2d}(s)\right)} \tag{41}$$

3.1.6 | Validation of the inner current loop modeling

To verify the inner current loop mathematical model of the studied system under PCMC, the same set up used previously is considered and the used external ramp amplitude is $V_m = 1$ V. The control to output transfer function ($\hat{\imath}_{ref}$ − to $-\hat{v}_{pv}$) frequency response are derived for two different irradiance values (200 and 1000 W/m²) and a fixed temperature value (25 °C) using both the previously derived mathematical model and the circuit-based switched model implemented in PSIM© software.

On one hand, as shown in FIGURE 7(a) and FIGURE 7(b), the frequency response are practically the same for the four models over the frequency range going from DC to one half the switching frequency, after incorporating the transfer function $H_{se}(s)$, for the different considered values of irradiance. On the other hand, the predictions of the mathematical modeling match very well with the switched model results from PSIM© software using the AC sweep tool for the same irradiance values. As a result, it would be convenient to choose the simplest model in further calculation or in designing the outer voltage loop controller. As shown in TABLE 9, Model 1 has the least number of gains and hence is the simplest one. Therefore, it will be used it in the rest of this work.

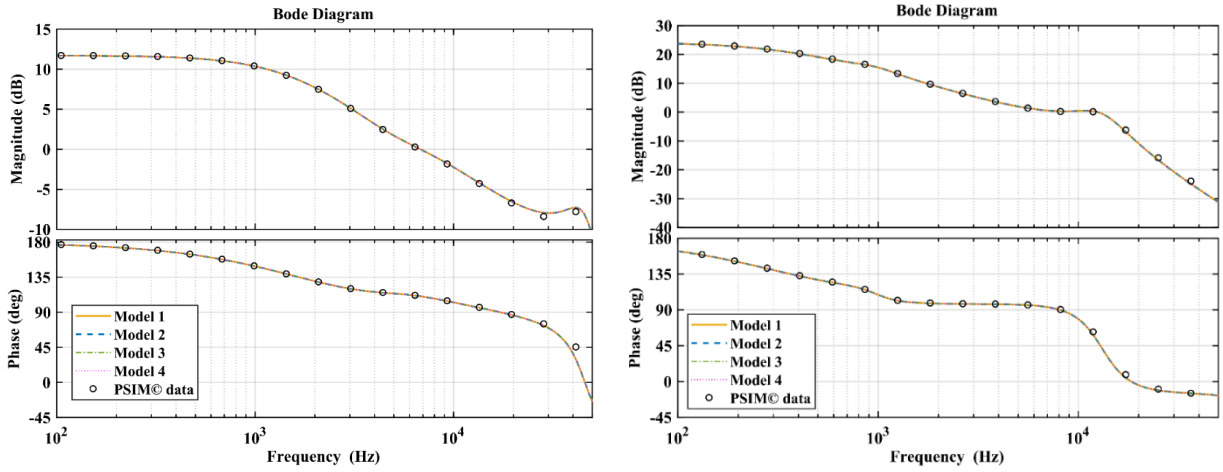

(a) (b)

FIGURE 7 Frequency response of $\hat{\imath}_{ref}$ −to−$\hat{v}_{pv}$ transfer function corresponding to: (a) 1000 W/m² and (b) 200 W/m² with fixed temperature value 25 °C.

The control to inductor ($\hat{\imath}_{ref}$ −to−$\hat{\imath}_{L1}$) transfer function is later derived by substituting $\hat{d}$ by its expression (35) in the first line of (34), while taking into consideration the sampling effect transfer function. The resulted transfer function writes:

$$\frac{\hat{\imath}_{L_1}(s)}{\hat{\imath}_{ref}(s)} = \frac{H_{id}(s)F_{m1}}{1 + F_{m1}\left(H_{se}(s)H_{id}(s) + F_{pv}H_{vd}(s)\right)} \tag{42}$$

In FIGURE 8(a) and FIGURE 8(b), the frequency response of the above transfer function is compared to the frequency response derived from PSIM© simulation using the AC sweep tool and as it can be observed, a very good matching is once more observed between the derived model and the circuit-based switched model implemented in PSIM© software.

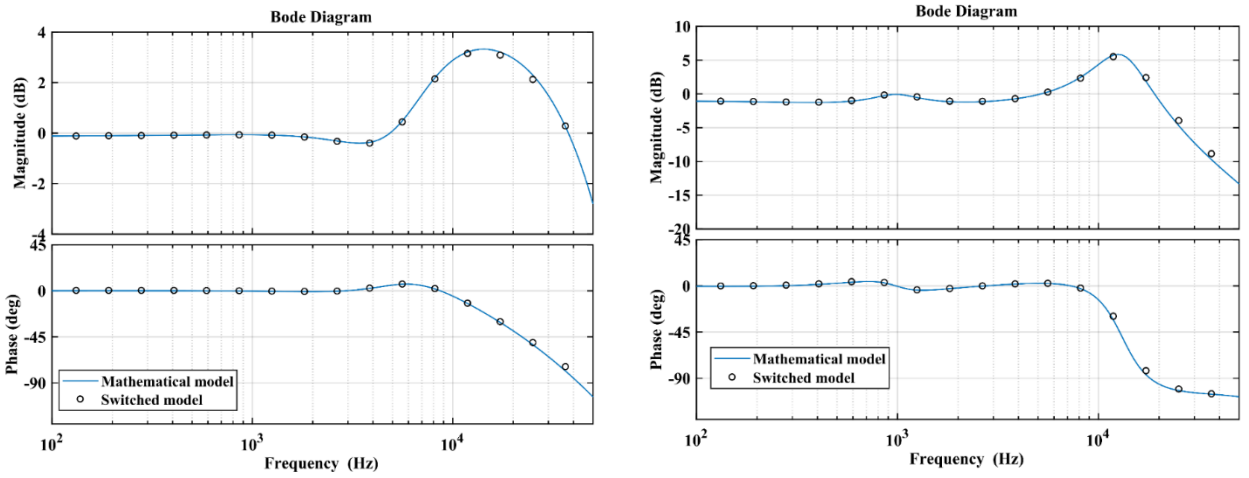

(a) (b)

FIGURE 8 Frequency response of $\hat{\imath}_{ref}$ −to−$\hat{\imath}_{L1}$ transfer function corresponding to: (a) 1000 W/m² and (b) 200 W/m² with fixed temperature value 25 °C.

3.2 | Outer voltage loop description and modeling

The ultimate objective of our PV-fed SEPIC controlling is to regulate the PV generator voltage to continuously track its MPP under variable environmental conditions. To achieve this goal, an outer voltage loop is inserted in cascade with the current mode controller. The outer voltage loop provides the current reference i_{ref} to the inner current loop. The block diagram of the system containing the outer voltage loop is depicted in FIGURE 9, where $G_c(s)$ is the transfer function of the voltage controller. In this block diagram Model 1 will be used. To design the outer voltage loop, the 'SmartCtrl' tool of PSIM© software was used. A simple PI controller, defined by (43), is considered for the outer voltage loop.

$$G_c(s) = K_p + \frac{K_i}{s} \tag{43}$$

where K_p is the proportional gain of the PI controller and K_i is its integral gain. The frequency response of the system including the inner current loop was performed for irradiance level of 200 W/m² and temperature 25 °C. Then, safe values of phase margin and crossover frequency were selected using the map

provided by the 'SmartCtrl' tool (199 ° and 1.3 kHz) and hence the gains of the PI controller were obtained. Finally, the whole system was implemented for simulation in PSIM© software.

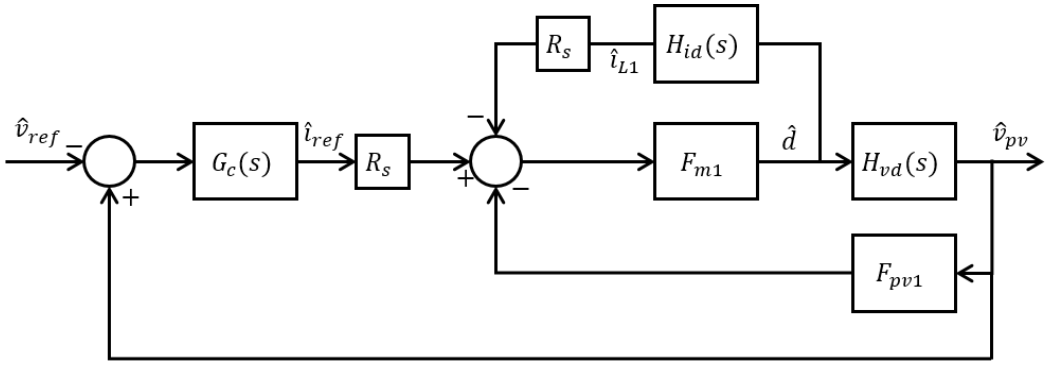

FIGURE 9 Block diagram of the two-loop controlled PV-fed SEPIC.

4 | Numerical simulations

PSIM© simulations were performed using the PV-fed SEPIC studied in the previous sections. P&O MPPT was used to extract the maximum power from the PV source and provide the reference voltage for the outer voltage loop. The sampling time for the MPPT controller was $T_{mppt} = 20$ ms and the voltage perturbation amplitude is $\Delta V = 0.2$ V. From the 'SmartCtrl' tool, the obtained PI controller gain is $K_p \approx 0.91$ and its integral gain is $K_i \approx 53834$. The sensing resistor is set to $R_s = 1\ \Omega$ and the external ramp amplitude value is $V_m = 1$ V. The resulting settling time is T_{Se} is in the range of 1 ms after each MPPT perturbation. It is worth to note that for any converter with current mode control, the settling time is shorter for the same converter with voltage mode control. For instance, for the same SEPIC of this study but with voltage mode control [46], the settling time could not be reduced below 5 ms using a type-III voltage controller. Consequently, the MPPT period was fixed to 20 ms and could not be made smaller than this value to avoid undesired interaction of the converter response with the dynamics of the MPPT algorithm. Here, the MPPT perturbation period can be selected shorter thanks to the use current mode control which in turns results in shorter settling time. With direct duty cycle control the situation is even worse than voltage mode control. For instance, in the simple low order boost converter considered in [15], the MPPT period was 100 ms while it could not be less than 50 ms in [29] after optimization. In [32], the MPPT period was 1 s with voltage mode control of a boost converter while it was 50 ms for the same converter with current mode control and series and parallel impedance emulation. Here, with the view of an experimental validation in which some hardware constriants prevents from reducing the MPPT perturbation period to small values, the MPPT period was fixed to 20 ms hence avoiding undesired interaction of the controlled system response with the dynamics of the MPPT algorithm while keeping in mind that an experimental validation would be possible with this value.

In order to test the robustness of the control scheme, the overall response of the system was evaluated for different irradiance and temperature sets. At first, the system was simulated under constant temperature (25 °C) and large step irradiance variation (from 200 W/m² to 600 W/m² and from 600 W/m² to 1000 W/m²). Then, fixed irradiance value (1000 W/m²) and variable temperature (from 10 °C to 25 °C and from 25 °C to 40 °C) were applied. Finally, both changing irradiance and temperature were considered. The results corresponding to these three scenarios are depicted in FIGURE 10(a), FIGURE 10(b), and FIGURE 10(c) respectively and they show that the system remains robust for large variation in the operating point and the maximum power of the PV generator is well tracked under the different considered atmospheric conditions.

The start-up response from zero initial conditions is also evaluated for the irradiance 200 W/m² and the temperature (25 °C) and the result is shown in

FIGURE 11. For this figure, the initial reference voltage for the P&O algorithm is $v_{ref} = 29.5$ V. The output of the PI voltage controller was limited to 10 V. At the beginning, the PV is working in constant current (CC) mode when the voltage increases linearly. Then there is a dip in the current while tracking the MPP. Therefore, after a startup transient, the PV voltage, power and current reach the steady-state within approximately 3 ms. When the MPPT algorithm starts working then the inner control loop is also functioning, therefore the inductor L_1 current starts to be controlled. The steady-state responses for irradiance 200 W/m² and 400 W/m² are depicted in FIGURE 12 and FIGURE 13 respectively showing a detailed view of the system response. As it can be noted, the PV voltage tracks tightly the reference voltage generated by the P&O algorithm. The PV power, as well, attains the desired MPP (≈ 47.8 W and ≈ 99 W). The PV current at MPP I_{mpp} and the average value of the inductor current I_{L1} are in accordance with the predicted values for the both cases.

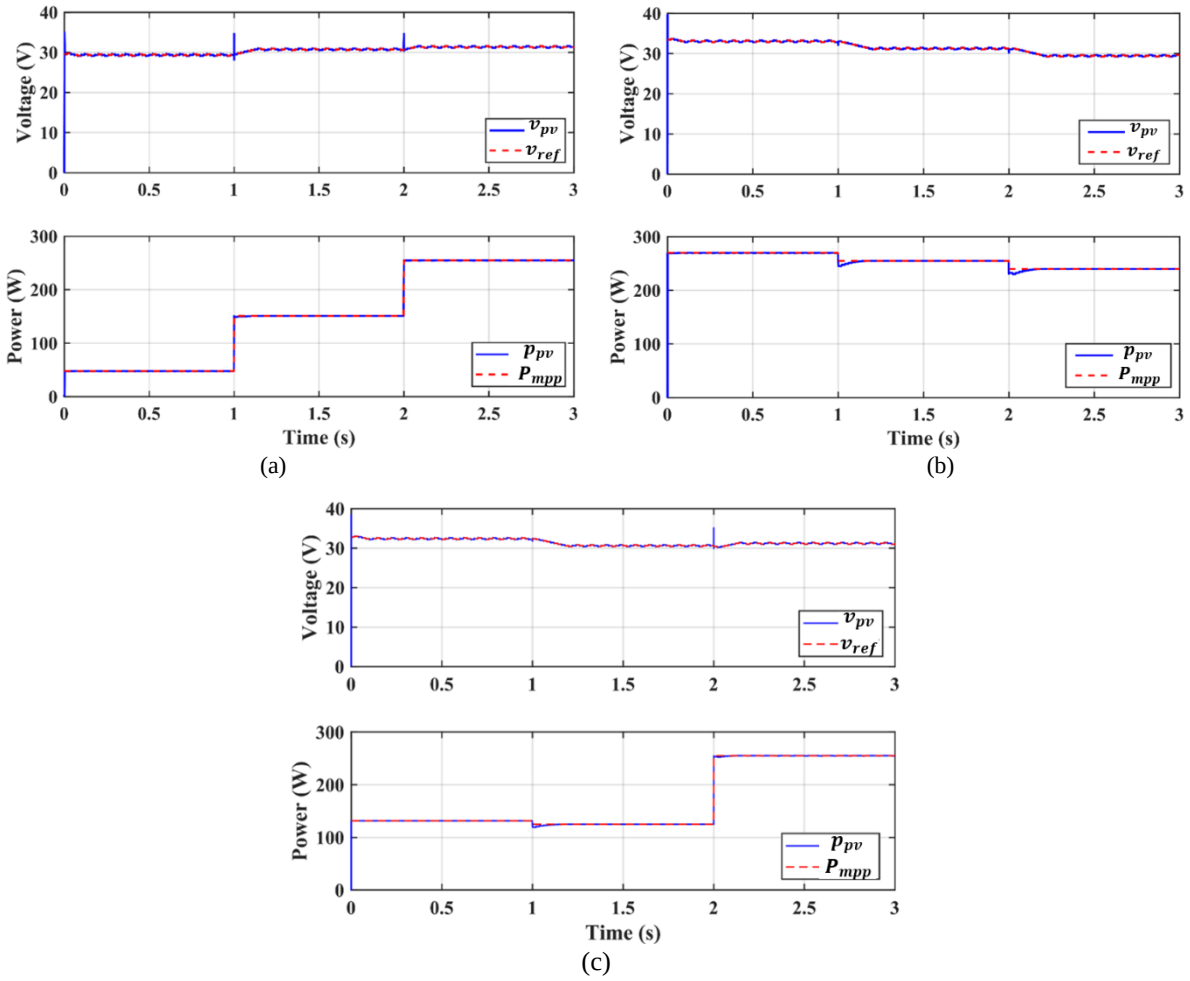

FIGURE 10 System response under PCMC for: (a) constant temperature: **25** °C and large step irradiance change: from **200** W/m² to **600** W/m² and from **600** W/m² to **1000** W/m², (b) constant irradiance: **1000** W/m² and large step temperature change: from **10** °C to **25** °C and from **25** °C to **40** °C and (c) variable irradiance: from **500** W/m² to **1000** W/m² at **2** s and variable temperature: from **10** °C to **25** °C at 1 s.

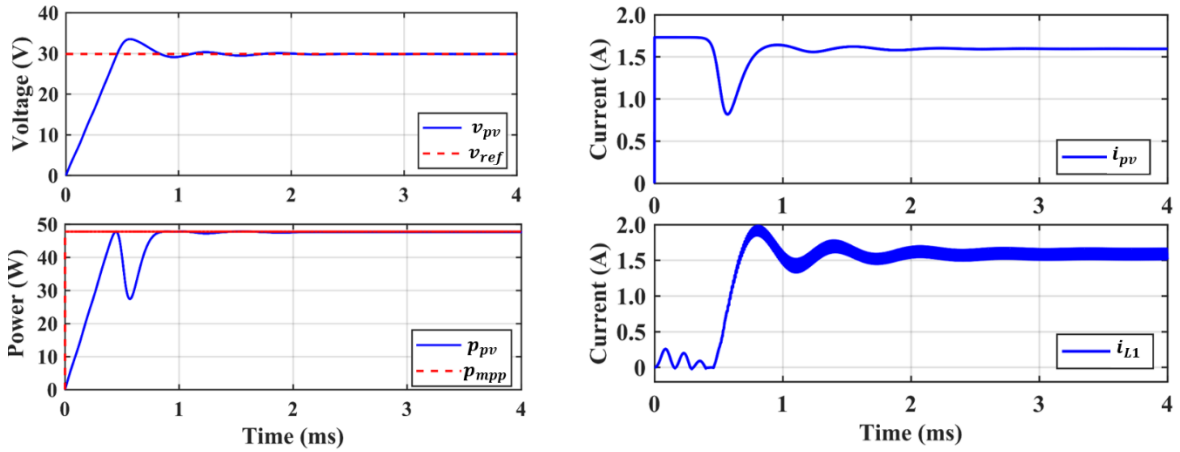

FIGURE 11 The start-up response for irradiance **200** W/m² and temperature (**25** °C).

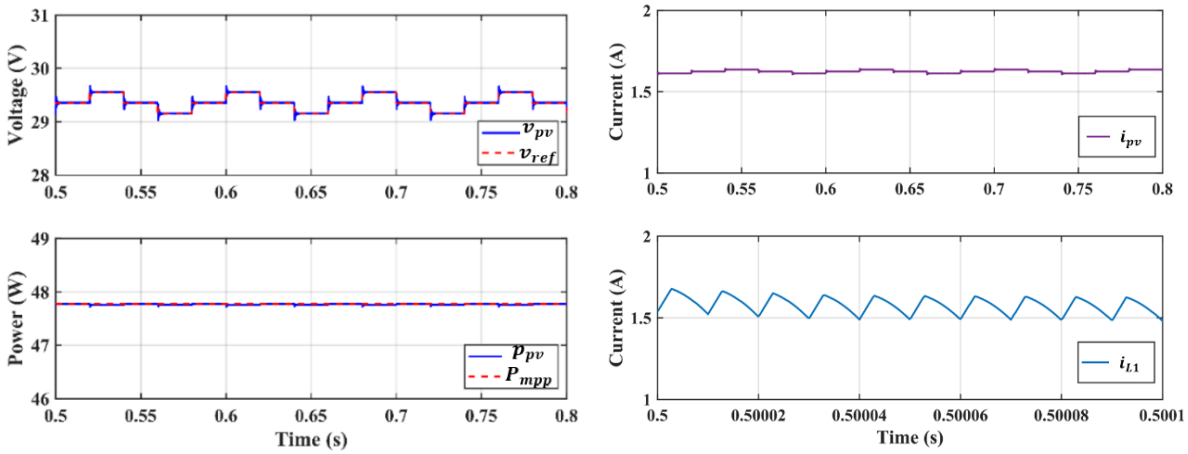

FIGURE 12 The steady-state response for irradiance **200** W/m² and temperature **25** °C.

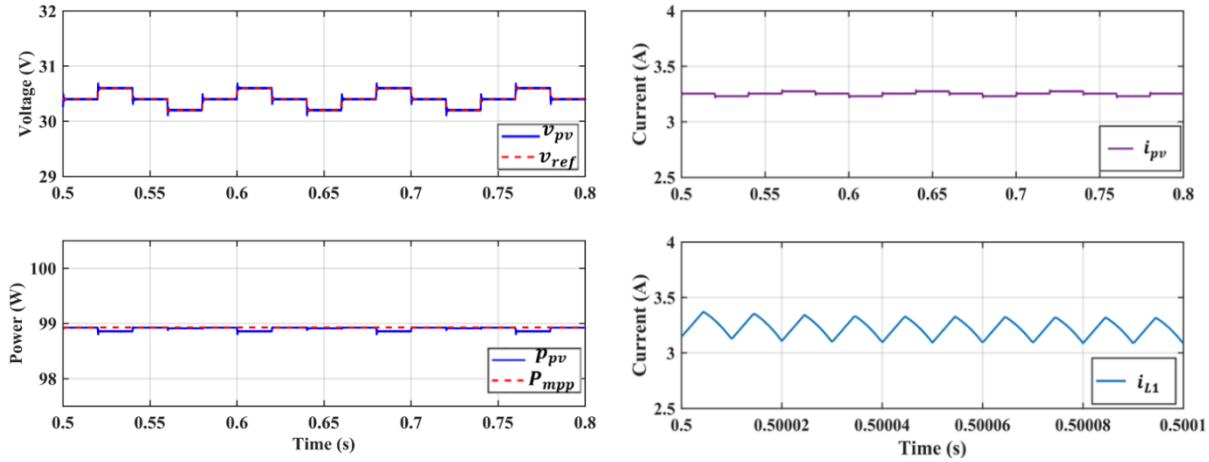

FIGURE 13 The steady-state response for irradiance **400** W/m² and temperature **25** °C.

5 | EXPERIMENTAL VALIDATION

In order to verify the validity of the mathematical findings and the numerical simulations, an experimental prototype has been constructed for almost the same set of parameter values with the inevitable nonidealities. The implemented power circuit and control circuit are shown in FIGURE 14 and FIGURE 15 respectively. The main switch S is realized by MOSFET C3M0120090D ($R_{DS(on)}$ = 0.12 Ω) with driver MAX4420. The power circuit consists of two inductors (L_1, L_2) made in the laboratory, three film capacitors (C_{pv}, C_1, C_2) with low Equivalent Series Resistance (ESR) and one Schottky diode C4D08120A with forward voltage drop 1.5 V. The inductor current i_{L1} is sensed using the current sensor LEM LA25 (bandwidth 150 kHz) with a unitary gain while the input voltage is sensed by a voltage divider with a gain of 0.05. The constant current load is realized by the electronic load EA-EL-3400-25 and the PV generator is realized by the solar array simulator E4360A. A picture of the overall experimental setup is depicted in FIGURE 16.

In the control circuit, the signal generator GwInstek MFG-2260M8 is used to get synchronized clock and ramp signals. For the realization of the error amplifier, the PI compensators, addition, subtraction and so on, the operational amplifier TL084 is used. The gains of the PI compensators are obtained from the values of capacitors and variable resistors around the op-amps. A 10 V Zener diode is used to prevent windup problem in integral action of PI controller. The comparator IC LM339 compares the reference current with the addition of ramp voltage and the sensed inductor current signal. For realization of S-R flip-flop, the IC CD4027 is used. At the start of the clock period, the output (pin 1) is set high with the rising transition of the clock (CLK) is applied at pin 7. Resetting of the output (pin 1) is accomplished by the high level of the comparator to the pin 4.

The MPPT part is programmed in the LAUNCHXL TMS320F28379D DSP of Texas Instruments. The sensed voltage v_{pv} and current i_{pv} signals are scaled down to the values supported by the DSP. To avoid loading effects, these signals are fed using buffer circuit. Moreover, the current i_{pv} is extracted after low pass filtering of inductor current i_{L1} so that no additional current sensor needed for this purpose. The samples of the state variables v_{pv} and i_{pv} are sent through ADC module and after calculation the signal is fed through the DAC for using it in the analog circuit. The signals are sampled at the switching frequency rate.

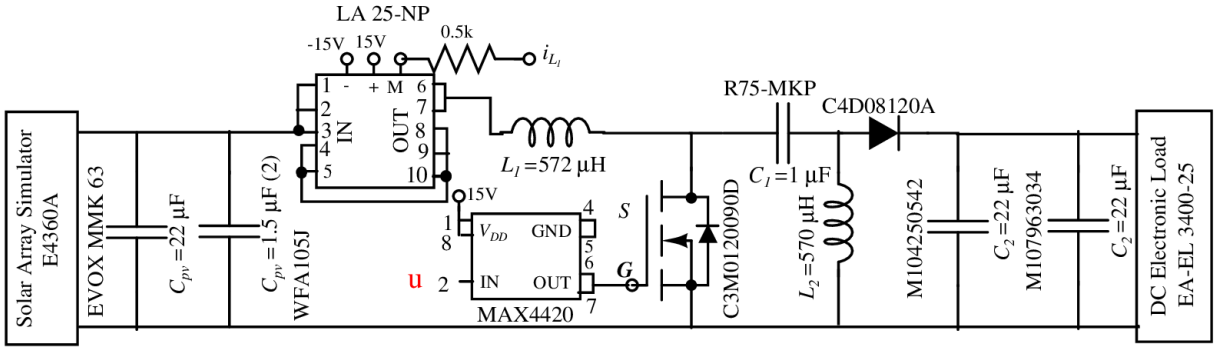

FIGURE 14 The implemented power stage circuit.

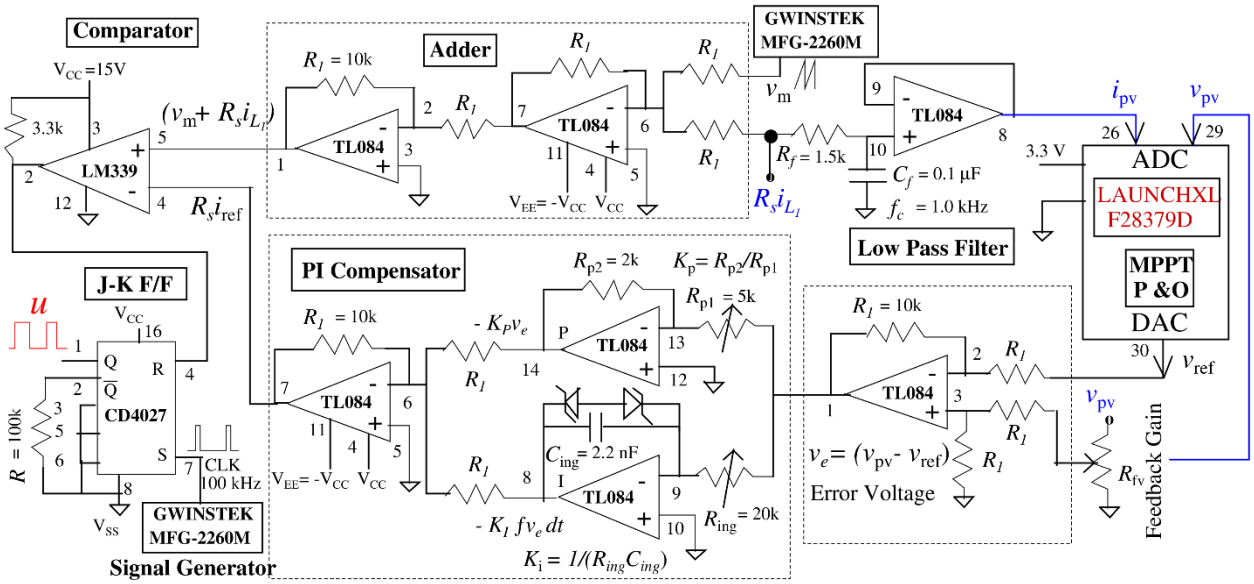

FIGURE 15 Schematic diagram of the power stage and control circuits with component type and values for the experimental setup.

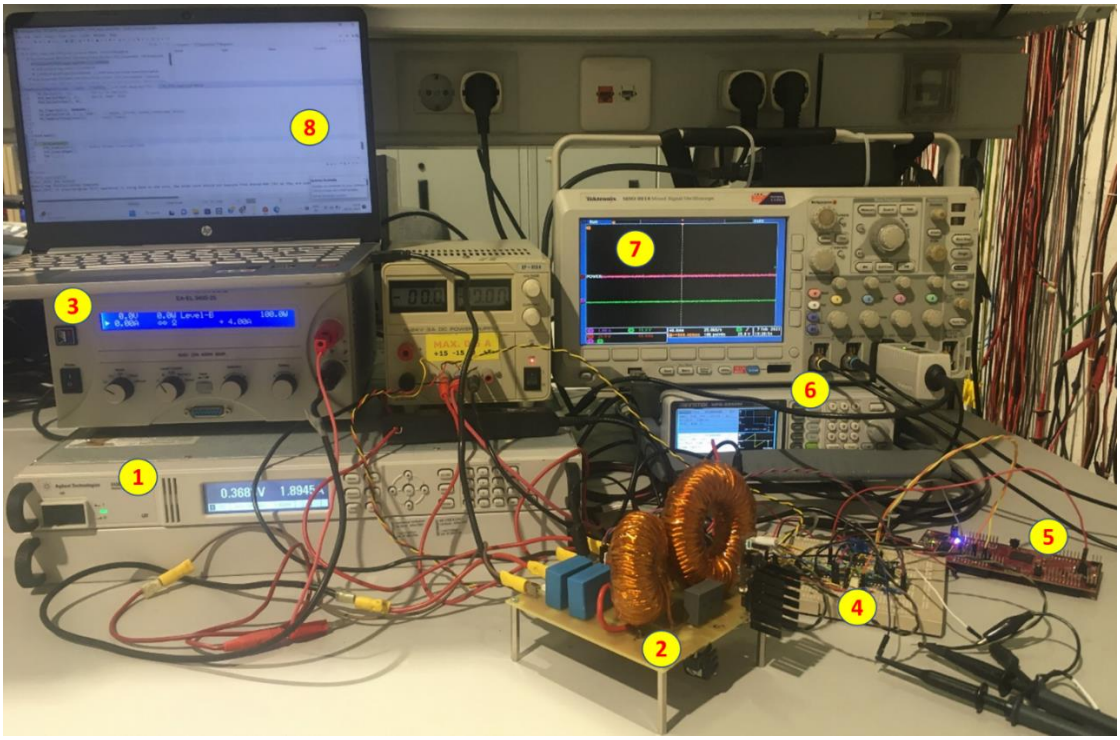

FIGURE 16 A picture of the overall experimental setup for validation. ① Solar array simulator E4360A, ② SEPIC power stage, ③ Electronic load EA-EL-3400-25, ④ Analog peak current mode control, ⑤ DSP TMS320F28379D with the P&O MPPT control, ⑥ Signal generator GwInstek MFG-2260M8, ⑦ Digital oscilloscope Tektronix MSO3014, ⑧ DSP programming.

The experimental waveforms shown below, have been captured using the mixed signal oscilloscope model Tektronix MSO3014 and the probes TEKTRONIX TCP0030A (bandwidth 120 MHz) for illustrating the

current waveforms. FIGURE 17(a) and FIGURE 17(b) show the waveforms of the PV voltage, current and power with constant temperature 25°C and for two different irradiance values (200 W/m² and irradiance 400 W/m²) corresponding to FIGURE 12 and FIGURE 13. The experimental waveforms are in good agreement with the theoretical predictions for the same set of parameter values and under the same conditions. The slight discrepancies are due to the nonidealities present in the components which are not considered in the simulation.

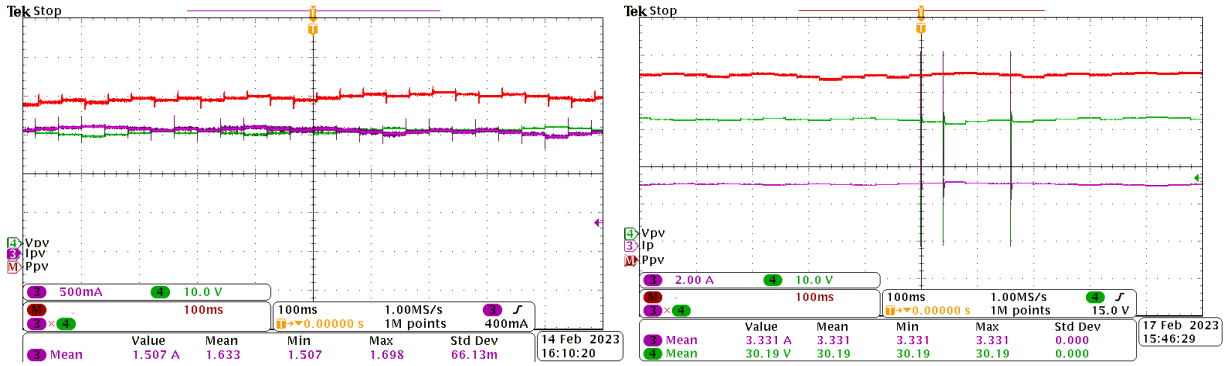

(a) (b)

FIGURE 17 waveforms with constant temperature 25 °C and: (a) irradiance 200 W/m² and (b) irradiance 400 W/m².

FIGURE 18(a) and FIGURE 18(b) display the waveforms of the PV voltage, current and power for the step variation in the irradiance (from 200 W/m² to 400 W/m² and from 400 W/m² to 200 W/m²).

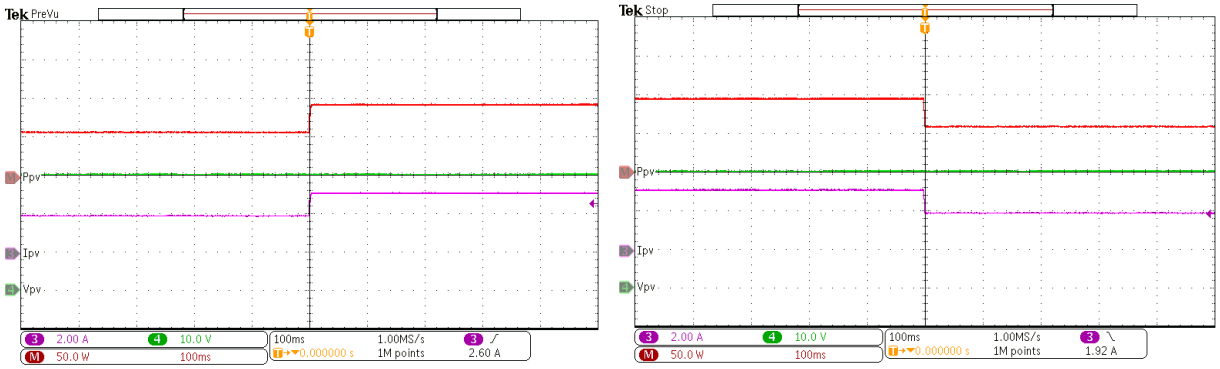

(a) (b)

FIGURE 18 waveforms with the constant temperature 25 °C and change in irradiance (a) 200 W/m² to 400 W/m² and (b) 400 W/m² to 200 W/m².

FIGURE 19(a) and FIGURE 19(b) show, respectively, the experimental and the simulated start-up response, for the irradiance 200 W/m² starting from zero initial conditions and with a limiter at the output of the PI compensator like in the numerical simulations of FIGURE 11.

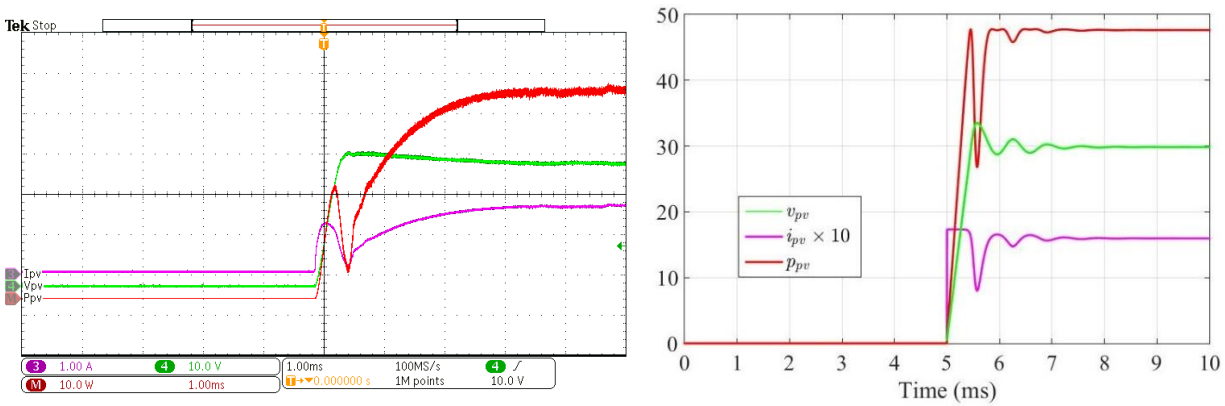

(a) (b)

FIGURE 19 the start-up response for irradiance 200 w/m² (a) experimental and (b) simulation.

6 | CONCLUSION

In the present paper a comprehensive dynamic modeling and a two-loop control of a PV-fed SEPIC were addressed. A steady-state analysis was performed mathematically and then validated by a circuit-based switched model implemented in PSIM© software. The mathematical transfer functions of the system were also derived mathematically and validated by the same software. The inner loop dictating the duty cycle of the PWM signal under PCMC scheme using the inductor current i_{L1} was modelled and analyzed. An outer voltage loop consisting of a PI controller was designed and used to generate the reference current to the inner loop. A detailed modeling of the inner loop was exposed. Four different models for the large signal of the inductor current feedback law were considered, from which the small-signal modeling of the inner loop was developed. The sampling effect transfer function was obtained for four approaches found in the literature. The resulted models were compared and it is found out that the ultimate transfer functions, after incorporating the sampling effect, give the same frequency response for the four approaches. Consequently, the simplest approach was selected for the rest of the modelling. The outer voltage design was carried out using the 'SmartCtrl' tool of PSIM© software. Hence, numerical simulations were performed using the same software where a standard PV panel was implemented with the PV-fed SEPIC under the complete two-loop control scheme. The results showed that the PV voltage is well tracked by the converter even under instantaneous step change in the environmental conditions hence demonstrating the robustness of the PV-fed SEPIC under PCMC. The designed PCMC was also validated using experimental measurements hence validating the theoretical findings and the numerical simulations.

ACKNOWLEDGMENTS

This work was carried out with the support of the National Center for Scientific and Technical Research of Morocco within the framework of the 'excellence scholarship' granted to Youssra Rais. Abdelali El Aroudi would like to acknowledge the support the Spanish Ministerio de Ciencia e Innovación under Grant PID2020-120151RB-I00. Kuntal Mandal would like to acknowledge the support received from the Agency for Management of University and Research Grants (AGAUR) under the Ministry of Research and Universities of the Government of Catalonia (Grant Reference No. 2020 BP 00260). Abdelali El Aroudi and Mohammed Al-Numay acknowledge financial support from the Researchers Supporting Project Number (RSP2023R150), King Saud University, Riyadh, Saudi Arabia.

ORCID

Youssra Rais https://orcid.org/0000-0002-8738-9914

Kuntal Mandal https://orcid.org/0000-0003-3977-652X

Alia Zakriti https://orcid.org/0000-0001-7644-7720

Abdellatif Khamlichi https://orcid.org/0000-0001-6954-774X

Mohammed Al-Numay https://orcid.org/0000-0001-8576-2060

Abdelali El Aroudi https://orcid.org/0000-0001-9103-7762

REFERENCES

1. Hao D, Qi L, Tairab AM, et al. Solar energy harvesting technologies for PV self-powered applications: A comprehensive review. *Renew Energy*. 2022;188:678-697. doi:10.1016/j.renene.2022.02.066
2. Kuo KC, Liao MS, Wang JC, et al. Comprehensive assessment of the long-term energy harvest capabilities for PV systems with different tilt angles: Case study in Taiwan. *Renew Sustain Energy Rev*. 2018;97(February 2017):74-89. doi:10.1016/j.rser.2018.08.024
3. Raj A, Arya SR, Gupta J. Solar PV array-based DC–DC converter with MPPT for low power applications. *Renew Energy Focus*. 2020;34(September):109-119. doi:10.1016/j.ref.2020.05.003
4. Rao CK, Patel R, Sahu LK, Gupta KK, Barwar MK. Maximum power point tracking controller implementation in multiple input converter for effective solar energy harvesting using maximum power point resistance method. *Int J Circuit Theory Appl*. 2023;51(1):302-321. doi:10.1002/cta.3428
5. Luo H, Wen H, Li X. Distributed MPPT control under partial shading condition. In: *2016 IEEE 8th International Power Electronics and Motion Control Conference, IPEMC-ECCE Asia 2016*. ; 2016:928-932. doi:10.1109/IPEMC.2016.7512411
6. Wang Q, Chen L, Hu M, Tang X, Li T, Ji S. Voltage prevention and emergency coordinated control strategy for photovoltaic power plants considering reactive power allocation. *Electr Power Syst Res*. 2018;163(April):110-115. doi:10.1016/j.epsr.2018.06.003
7. Jafarian H, Kim N, Parkhideh B, Enslin J. Analysis of smart inverter functions of decentralized grid-connected AC-stacked PV inverter architecture. *Conf Proc - IEEE Appl Power Electron Conf Expo - APEC*. Published online 2017:3594-3600. doi:10.1109/APEC.2017.7931214
8. Sharma P. Characterization of High Concentration Photovoltaic Systems Using Multijunction Solar Cells. Published online 2017.
9. Limsakul C, Songprakorp R, Sangswang A, Parinya P. Impact of Photovoltaic Grid-Connected Power Fluctuation on System Frequency Deviation in Contiguous Power Systems. In: *IECON 2015 - 41st Annual Conference of the IEEE Industrial Electronics Society*. ; 2015:3236-3241.

10. Kofinas P, Dounis AI, Papadakis G, Assimakopoulos MN. An Intelligent MPPT controller based on direct neural control for partially shaded PV system. *Energy Build*. 2015;90(2015):51-64. doi:10.1016/j.enbuild.2014.12.055

11. Prabaharan N, Palanisamy K. Analysis and integration of multilevel inverter configuration with boost converters in a photovoltaic system. *Energy Convers Manag*. 2016;128:327-342. doi:10.1016/j.enconman.2016.09.088

12. Loukriz A, Haddadi M, Messalti S. Simulation and experimental design of a new advanced variable step size Incremental Conductance MPPT algorithm for PV systems. *ISA Trans*. 2016;62:30-38. doi:10.1016/j.isatra.2015.08.006

13. Selmi T, Abdul-Niby M, Devis L, Davis A. P&O MPPT implementation using MATLAB/Simulink. In: *2014 9th International Conference on Ecological Vehicles and Renewable Energies, EVER 2014*. ; 2014. doi:10.1109/EVER.2014.6844065

14. Nedumgatt JJ, Jayakrishnan KB, Umashankar S, Vijayakumar D, Kothari DP. Perturb and observe MPPT algorithm for solar PV systems-modeling and simulation. In: *Proceedings - 2011 Annual IEEE India Conference: Engineering Sustainable Solutions, INDICON-2011*. ; 2011. doi:10.1109/INDCON.2011.6139513

15. Elgendy MA, Zahawi B, Atkinson DJ. Assessment of perturb and observe MPPT algorithm implementation techniques for PV pumping applications. *IEEE Trans Sustain Energy*. 2012;3(1):21-33. doi:10.1109/TSTE.2011.2168245

16. Ahmad J. A fractional open circuit voltage based maximum power point tracker for photovoltaic arrays. In: *Software Technology and Engineering (ICSTE), 2010 2nd International Conference On*. Vol 1. ; 2010:247-250. doi:10.1109/ICSTE.2010.5608868

17. Murtaza a. F, Sher H a., Chiaberge M, Boero D, Giuseppe MD, Addoweesh KE. A novel hybrid MPPT technique for solar PV applications using perturb & observe and Fractional Open Circuit Voltage techniques. In: *MECHATRONIKA, 2012 15th International Symposium*. ; 2012:1-8.

18. Baimel D, Shkoury R, Elbaz L, Tapuchi S. Novel Optimized Method for Maximum Power Point Tracking in PV Systems Using Fractional Open Circuit Voltage Technique. In: *International Symposium on Power Electronics, Electrical Drives, Automation and Motion*. Vol 2. ; 2016:889-894. doi:10.1109/SPEEDAM.2016.7525984

19. Putri RI, Wibowo S, Rifa'i M. Maximum power point tracking for photovoltaic using incremental conductance method. *Energy Procedia*. 2015;68:22-30. doi:10.1016/j.egypro.2015.03.228

20. Islam MA, Kabir MA. Neural network based maximum power point tracking of photovoltaic arrays. In: *TENCON 2011 2011 IEEE Region 10 Conference*. ; 2011:79-82. doi:10.1109/TENCON.2011.6129067

21. Rai AK, Kaushika ND, Singh B, Agarwal N. Simulation model of ANN based maximum power point tracking controller for solar PV system. *Sol Energy Mater Sol Cells*. 2011;95(2):773-778. doi:10.1016/j.solmat.2010.10.022

22. Roy RB, Basher E, Yasmin R, Rokonuzzaman M. Fuzzy logic based MPPT approach in a grid connected photovoltaic system. In: *The 8th International Conference on Software,*

Knowledge, Information Management and Applications (SKIMA 2014). Vol 1. ; 2014:1-6. doi:10.1109/SKIMA.2014.7083525

23. Díaz Martínez D, Trujillo Codorniu R, Giral R, Vázquez Seisdedos L. Evaluation of particle swarm optimization techniques applied to maximum power point tracking in photovoltaic systems. *Int J Circuit Theory Appl*. 2021;49(7):1849-1867. doi:10.1002/cta.2978
24. Kumar P, Jain G, Palwalia DK. Genetic algorithm based maximum power tracking in solar power generation. In: *2015 International Conference on Power and Advanced Control Engineering (ICPACE)*. ; 2015:1-6. doi:10.1109/ICPACE.2015.7274907
25. Taghvaee MH, Radzi MAM, Moosavain SM, Hizam H, Hamiruce Marhaban M. A current and future study on non-isolated DC-DC converters for photovoltaic applications. *Renew Sustain Energy Rev*. 2013;17:216-227. doi:10.1016/j.rser.2012.09.023
26. Salvador TC, Tofoli FL, de Souza Oliveira Júnior D, Ribeiro ER. Nonisolated high step-up DC-DC interleaved SEPIC converter based on voltage multiplier cells. *Int J Circuit Theory Appl*. 2022;50(8):2735-2758. doi:10.1002/cta.3307
27. Chandra S, Gaur P. An efficient switched inductor–capacitor-based novel non-isolated high gain SEPIC for solar energy applications. *Int J Circuit Theory Appl*. 2022;(July 2022):1286-1312. doi:10.1002/cta.3454
28. Femia N, Petrone G, Spagnuolo G, Vitelli M. A technique for improving P&O MPPT performances of double-stage grid-connected photovoltaic systems. *IEEE Trans Ind Electron*. 2009;56(11):4473-4482. doi:10.1109/TIE.2009.2029589
29. Femia N, Petrone G, Spagnuolo G, Vitelli M. Optimization of Perturb and Observe Maximum Power Point Tracking Method. *IEEE Trans Power Electron*. 2005;20(4):963-973. doi:10.1109/TPEL.2005.850975
30. Xiao W, Dunford WG, Palmer PR, Capel A. Regulation of photovoltaic voltage. *IEEE Trans Ind Electron*. 2007;54(3):1365-1374. doi:10.1109/TIE.2007.893059
31. Garcerá G, González-Medina R, Figueres E, Sandia J. Dynamic modeling of DC – DC converters with peak current control in double-stage photovoltaic grid-connected inverters. *Int J CIRCUIT THEORY Appl*. 2012;40(8):793-813. doi:10.1002/cta
32. Urtasun A, Samanes J, Barrios EL, Sanchis P, Marroyo L. Control of a Photovoltaic Array Interfacing Current-Mode-Controlled Boost Converter Based on Virtual Impedance Emulation. *IEEE Trans Ind Electron*. 2019;66(5):3496-3506. doi:10.1109/TIE.2018.2856192
33. Bianconi E, Calvente J, Giral R, et al. A fast current-based MPPT technique employing sliding mode control. *IEEE Trans Ind Electron*. 2013;60(3):1168-1178. doi:10.1109/TIE.2012.2190253
34. Mamarelis E, Petrone G, Spagnuolo G. Design of a sliding-mode-controlled SEPIC for PV MPPT applications. *IEEE Trans Ind Electron*. 2014;61(7):3387-3398. doi:10.1109/TIE.2013.2279361
35. Cabal C, Martínez-Salamero L, Séguier L, Alonso C, Guinjoan F. Maximum power point tracking based on slidingmode control for output-series connected converters in

photovoltaic systems. *IET Power Electron*. 2014;7(4):914-923. doi:10.1049/iet-pel.2013.0348

36. Hussain J, Mishra MK. Design of current mode controlled SEPIC DC-DC converter for MPPT control of wind energy conversion systems. In: *4th IEEE Sponsored International Conference on Computation of Power, Energy, Information and Communication, ICCPEIC 2015*. ; 2015:177-182. doi:10.1109/ICCPEIC.2015.7259460

37. Zhou G, Xu J, Wang J. Constant-frequency peak-ripple-based control of buck converter in CCM: Review, unification, and duality. *IEEE Trans Ind Electron*. 2014;61(3):1280-1291. doi:10.1109/TIE.2013.2257143

38. Yan Y, Lee FC, Mattavelli P, Liu PH. I2 average current mode control for switching converters. *IEEE Trans Power Electron*. 2014;29(4):2027-2036. doi:10.1109/TPEL.2013.2265381

39. Cantillo A, De Nardo A, Femia N, Zamboni W. Stability issues in peak-current-controlled SEPIC. *IEEE Trans Power Electron*. 2011;26(2):551-562. doi:10.1109/TPEL.2010.2066288

40. Chiang SJ, Shieh HJ, Chen MC. Modeling and control of PV charger system with SEPIC converter. *IEEE Trans Ind Electron*. 2009;56(11):4344-4353. doi:10.1109/TIE.2008.2005144

41. Middlebrook RD. Topics in Multiple-Loop Regulators and Current- Mode Programning. *IEEE Trans POWER Electron*. 1987;PE-2(2):109-124.

42. Ridley RB. A New, Continuous-Time Model For Current-Mode Control. *IEEE Trans POWER Electron*. 1991;6(2):271-280.

43. Verghese GC, Bruzos CA, Mahabir KN. Averaged and sampled-data models for current mode control: A reexamination. In: *20th Annual IEEE Power Electronics Specialists Conference*. ; 1989:484-491.

44. Tan FD, Middlebrook RD. A Unified Model for Current-Programmed Converters. *IEEE Trans Power Electron*. 1995;10(4):397-408. doi:10.1109/63.391937

45. Haroun R, El Aroudi A. Analysis, design, and simulation of a dual active bridge for PV-based residential nanogrids. In: *2020 5th International Conference on Renewable Energies for Developing Countries, REDEC 2020*. ; 2020. doi:10.1109/REDEC49234.2020.9163840

46. Rais Y, El Aroudi A, Zakriti A, Khamlichi A. Modeling and design of voltage-mode controlled PV-fed SEPIC converter. *IFAC-PapersOnLine*. 2022;55(12):514-519. doi:10.1016/j.ifacol.2022.07.363

47. W. Erickson R, Maksimović D. *Fundamentals of Power Electronics*. Vol Third edit.; 2020. doi:10.1007/978-1-4471-5104-3_2

48. Tan FD, Middlebrook R. Unified Modeling and Measurement of Current-Programmed Converters. In: *Proceedings of IEEE Power Electronics Specialist Conference - PESC '93*. ; 1993:380-387.